Fundamental Proximity Effects in Focused Electron Beam Induced Deposition

Harald Plank,[†,‡,*] Daryl A. Smith,[§] Thomas Haber,[‡] Philip D. Rack,[§,⊥] and Ferdinand Hofer[†,‡]

[†]Institute for Electron Microscopy, Graz University of Technology, Steyrergasse 17, 8010 Graz, Austria, [‡]Center for Electron Microscopy, Steyrergasse 17, 8010 Graz, Austria, [§]Materials Science and Engineering, The University of Tennessee, 603 Dougherty Hall, Knoxville, Tennessee 37996-2200, United States, and [⊥]Center for Nanophase Materials Sciences, Oak Ridge National Laboratories, Oak Ridge, Tennessee 37831, United States

ABSTRACT Fundamental proximity effects for electron beam induced deposition processes on nonflat surfaces were studied experimentally and *via* simulation. Two specific effects were elucidated and exploited to considerably increase the volumetric growth rate of this nanoscale direct write method: (1) increasing the scanning electron pitch to the scale of the lateral electron straggle increased the volumetric growth rate by 250% by enhancing the effective forward scattered, backscattered, and secondary electron coefficients as well as by strong recollection effects of adjacent features; and (2) strategic patterning sequences are introduced to reduce precursor depletion effects which increase volumetric growth rates by more than 90%, demonstrating the strong influence of patterning parameters on the final performance of this powerful direct write technique.

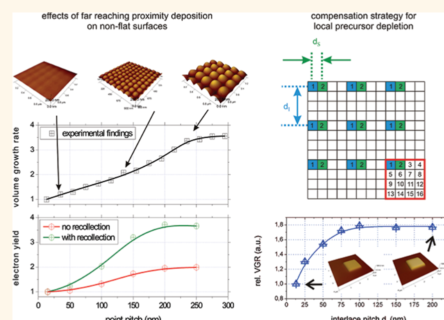

KEYWORDS: electron beam induced deposition · Monte Carlo simulation · nanotechnology · platinum · patterning

During the past decade, focused electron beam induced deposition (EBID)[1−4] has attracted more and more attention since it represents a very powerful direct write method for the three-dimensional fabrication of functional nanostructures (conductive, insulating, magnetic, *etc.*) even on nonflat surfaces.[5−13] In contrast to focused ion beam induced deposition,[3] which is an often used technique, EBID is free of sputtering effects, unwanted ion implantation, and the partly high thermal stress which can alter or harm the substrate.[14−17] Due to these advantages, EBID is highly suited for rapid prototyping with particular emphasis on sensitive samples such as soft matter (polymers, biological samples, *etc.*), nanoelectronic and optical applications, or proof of concept studies.[18−26]

However, due to the three-dimensional propagation of electrons in solids,[27] primary electrons are not confined to the point of beam incidence, which broadens the intended deposition point[28−31] and limits the minimum achievable feature dimension as a function of primary electron energy and deposit height.[28,32,33,36] Furthermore, scattered electrons can also leave the deposit again and cause proximity deposition, as observed as an unwanted effect on the nanoscale by several authors,[32,34−37] which reduces the lateral resolution capabilities of EBID even further. The understanding of the mechanism of proximity effects is an essential part for both, reducing unwanted proximity deposition or possibly using such processes as an advantage for special purposes.

In this study, we focus on fundamental proximity effects for nonflat deposits as can be used for template purposes[38−43] or functional structures.[37,44−52] We combine experimental results with Monte Carlo electron trajectory simulations[2,53] as the method of choice for determining the individual effects of different electron species such as backscattered and forward scattered electrons. The combination of both approaches enables us to interpret the observed proximity effects by fundamental processes which are of relevance for all electron beam induced processes independent of the used precursor gas. The study demonstrates clearly that a careful experimental parameter adaptation is absolutely necessary in order to exploit the full potential of this powerful direct write synthesis technique by means of maximization of deposition efficiencies and minimization of structure broadening and unwanted proximity deposition.

* Address correspondence to harald.plank@felmi-zfe.at.

Received for review September 15, 2011 and accepted December 19, 2011.

Published online December 19, 2011
10.1021/nn204237h

© 2011 American Chemical Society

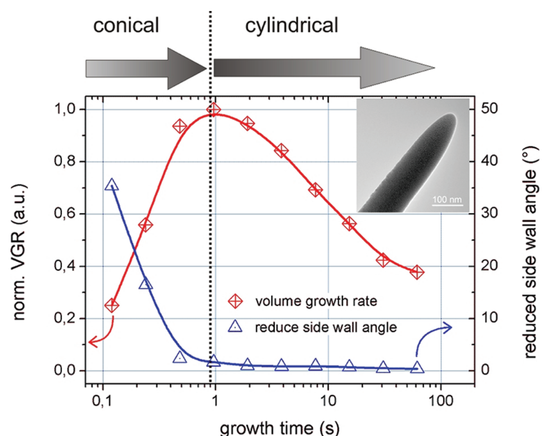

Figure 1. Temporal evolution of volume growth rate (diamonds, left axis) and reduced side wall angle (triangles, right axis), measured to the surface normal, for free-standing Pt nanopillars grown at 5 keV/1600 pA in spot mode. The inset shows a TEM bright field image of a nanopillar revealing the typical conical geometry followed by the cylindrical shape with a diameter of ∼120 nm.

RESULTS AND DISCUSSION

Classical EBID patterning strategies typically use a raster- or serpentine-like sequence of consecutive discrete deposition events with the point pitch *d* (assumed to be identical in *X* and *Y*) and the beam dwell time *t* per point (assumed to be constant for all points). After completing a single patterning frame, the number of patterning loops is used to adjust the deposit thickness. Typical instrumental default conditions are often chosen in such a way that the resulting surface roughness of the deposits is very low (atomic force microscopy measurements reveal values of 1 nm (rms) or less). However, the resulting volume growth rates (VGRs) for such default conditions are often rather low, which is caused by the fact that deposition is mainly caused by primary electrons (PE) at the point of incidence, backscattered electrons (BSE) in the vicinity of the incident electron beam, and by related secondary electrons type I and II (SE_I, SE_{II}).[28,30,53] Many primary and subsequently generated electrons in the solid, however, are "lost" within the bulk according to the interaction volume,[27] which results in very low deposition efficiencies. This is demonstrated in Figure 1, which shows the temporal VGR evolution (diamonds, left axis) of a free-standing Pt nanopillar (representing a single pixel of a scanned pattern), fabricated from $MePtCpMe_3$ precursor at 5 keV and 1600 pA on HOPG substrates in spot mode. For growth times (respective dwell times) in the microsecond range, the VGR is very low due to the high number of "lost" electrons as the primary electron penetrates into the substrate and few of the generated secondary electrons along its trajectory make it to the surface. As the growth time increases, the deposit develops into a conical regime, which is characterized by a change in side wall angle (triangles, right axis) from initially 90° from the flat substrate. As the cone develops, the VGR increases strongly as more electrons traverse the surface (scattered primary electrons and generated secondary electrons) and cause more deposition events on the deposit surface.[2,31,32] Once the interaction volume reaches the substrate/pillar interface, the VGR is maximized and the morphology changes into the cylindrical regime,[28,32,53,54] which is reflected by the saturation of the reduced side wall angle. The inset in Figure 1 shows a transmission electron microscopy (TEM) bright field image which reveals the top conical interaction region and the saturated cylindrical region, in this case with a cylinder diameter of about 120 nm. The decreasing VGR tendency after this maximum is related to the kinetics of the precursor molecules along the nanopillar and has been described in literature.[29,30,54]

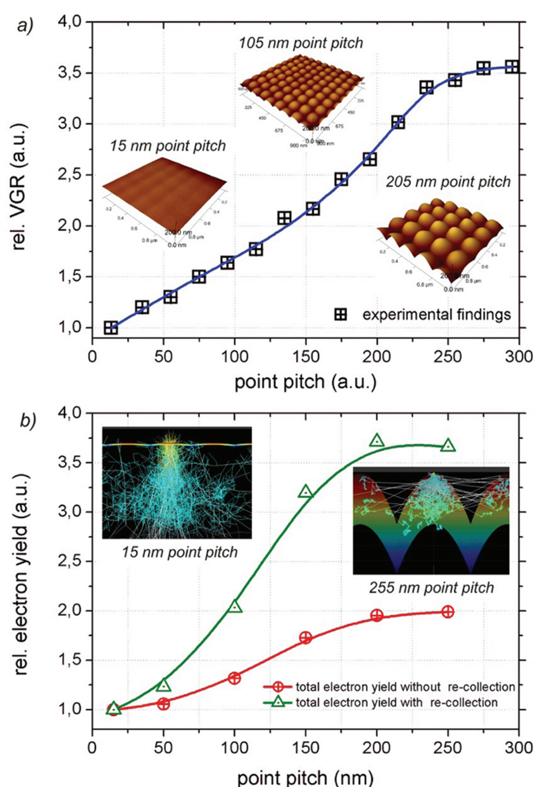

Figure 2. (a) Experimental volume growth rate (VGR) dependency (squares) on patterning point pitches with AFM images as insets revealing the changing surface properties (identical scales). (b) Monte Carlo based simulations of relative electron yield for surface penetrating electrons (BSE + FSE) without (circles) and with electron recollection (triangles). The insets show electron trajectories on almost flat (left inset) and multidome surfaces revealing origin of enhanced electron emission and recollection.

Volume Growth Rate Variation. According to Figure 1, it would be necessary to allow each single point or pixel to develop into a conical morphology to make the otherwise "lost" electrons accessible for deposition events. To reveal this proposed VGR efficiency increase, the patterning point pitch *d* during deposition was

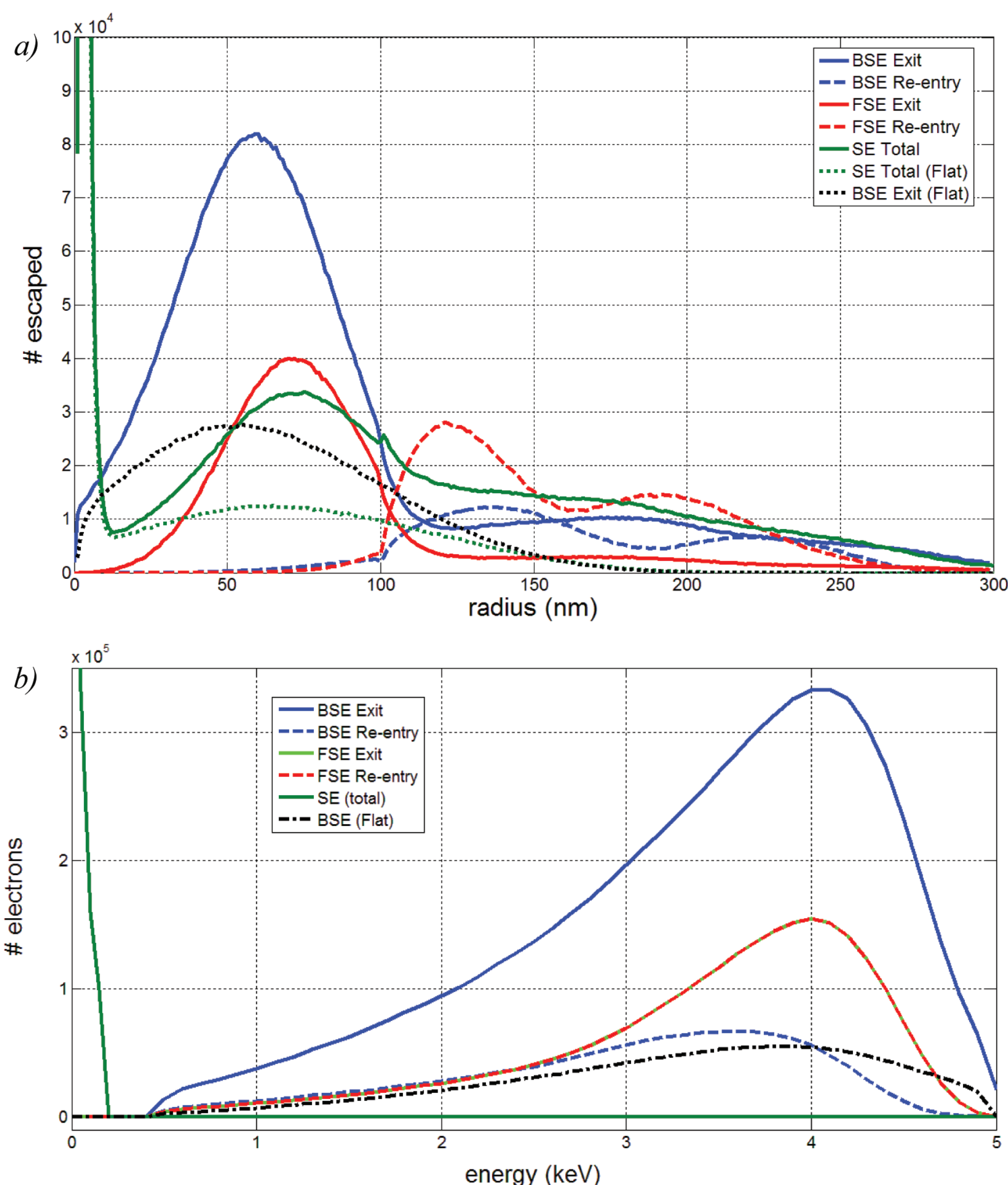

Figure 3. Monte Carlo based histograms of surface penetration events *versus* (a) radial distance to the electron beam and (b) electron energy for surface exiting BSE and FSE as well as for recollected BSE and FSE compared for flat and multidome surfaces according to a patterning point pitch of 200 nm.

continuously increased while the dwell time and the total electron dose per unit area was kept constant *via* changing the number patterning loops. The Pt deposits have then been characterized *via* focused ion beam (FIB) cross cuts and scanning electron microscopy (SEM). As expected, the increasing point pitch leads to increasing deposit volumes after identical deposition times (and electron dose), as shown in Figure 2a, by a relative VGR plot, referenced to the default conditions of 13 nm point pitch. The insets show atomic force microscopy (AFM) height images which visualize the change from flat surfaces (13 nm pitch) toward multidome surfaces (200 nm pitch). Note, the deposit volumes used for the VGR calculations do not include the dome itself but just the fully closed part underneath (see S1 in Supporting Information), hence, underestimating the real VGR values (see Figure S1c). To give confirmation that the structures have a fully closed character, free-standing single lines were characterized by transmission electron microscopy (TEM) which revealed a closed character even for point pitches beyond 300 nm S1 and Figure S2. Furthermore, the three-dimensional deposits on HOPG have been carefully characterized *via* SEM from different geometries (Figure S2) and revealed the appearance of pinholes along the diagonals between pixels for point pitch values above 250 nm, hence, representing the upper point pitch limit for continuous or fully closed

deposits. It is of particular interest to compare the fully closed character of a 255 nm point pitch deposit with the typical diameter of a free-standing Pt nanopillar of about 120 nm, which is grown at identical electron energy and beam current in spot mode (see Figure 1). It reflects that the lateral growth rate is increased by more than 150% just because of proximity effects which can be seen as an advantage (higher VGR) but also as a disadvantage due to unwanted structure broadening.

To explain the strong VGR increase shown in Figure 2a, two main effects must be considered: (1) a change in the growth regime, based on varying precursor depletion/replenishment conditions;[3,29,30,37,54,55] and (2) electron trajectory related proximity deposition. The latter effect is rather complex since not only PE, BSE, SE_I, and SE_{II} are involved but also forward scattered electrons (FSE) and related SE which are further denoted as SE_{III}. Figure 2b shows simulated and normalized electron yield for PtC_4 *versus* pitch considering electrons that only exit a dome (circles) and including electrons that re-enter neighboring domes (triangles). Additionally, due to the composition changes that will be demonstrated below, we also simulated PtC_7 whose normalized total electron yield *versus* pitch is found to be nearly identical to PtC_4, though the absolute value for high point pitches is slightly increased due to the smaller average atomic number and molecular weight (see Figure S4a and S4). While all the subsequent discussion will focus on the simulated PtC_4 results, the data are consistent with slightly changing PtC_X composition described below. Figure 3a shows Monte Carlo based histograms for surface exiting FSEs (solid red) and BSEs (solid blue) *versus* the projected radial distance to the primary electron beam for a multidome surface based on 200 nm point pitch patterns in comparison to the BSE distribution for flat surface (black, dash dotted) (details can be found in S3). The integrated BSE yield (excluding re-entered electrons) is increased by a factor of 2.57 (BSE_{200}/BSE_{15}, integrated for the full lateral range simulated) which is caused by the enhanced surface area which folds closely around the intrinsic interaction volume.[27] Furthermore, the curved surfaces allow for considerable FSE contributions: the 200 nm point pitch surfaces generate about 1.9 (FSE_{200}/BSE_{15}, integrated for the full lateral range simulated) times the BSE yield for flat surfaces. More importantly, however, is the fact that surface exiting FSEs are not "lost" but entirely recollected by adjacent domes. This recollection contribution holds also for a certain fraction of BSEs depending on their exit angles. Such recollected BSEs and FSEs can be re-emitted again (eventually dissociating a precursor molecule) or have their remaining energy loss entirely within the adjacent dome. Figure 3a shows also the recollection contributions for BSEs (dashed blue) and FSEs (dashed red) which show considerable contribution even at a distance of 200 nm apart from the actual primary electron beam entry. In this context, it is important to note that such far reaching electrons have often experienced a high number of inelastic scattering events which decrease the electron energy and increases the dissociation probability due to the energy-dependent dissociation probability for precursor molecules.[28−30,55,56] In addition to this "long distance" BSE and FSE contribution with increasing deposition probability, near surface SE generation (types I, II, and III) can also strongly contribute to deposition due to their low energies. Figure 3a depicts also the radial distribution of the total SE yield for flat (green dotted) and multidome surfaces (solid green; based on 200 nm point pitch patterns) which were found to increase with the same tendency as the sum of BSE and FSE, while the relative SE fraction is decreasing from about 50% to less than 30% for 15 and 250 nm point pitches, respectively (see S4 and Figure S4).

Figure 3b shows the energy distribution of surface penetrating FSE and BSE (see color code) for the 200 nm point pitch pattern in comparison to the BSE related energy distribution (black dash-dot line). Although qualitatively similar, it can be seen that the absolute number of low energy electrons is strongly increased as a result of far reaching BSE and FSE which favors deposition events even further due to the previously mentioned energy dependent dissociation probability.

Figure 2b gives finally the sum of surface exiting BSE, FSE, and SE (all species) *versus* point pitches in a relative plot (referenced to 15 nm pitch) without (circles) and with (triangles) recollected electron contributions, clearly indicating the strong increase due to multiple surface penetration events (up to an additional factor of 2). As it can be seen, a saturation tendency is observed for point pitches beyond 200 nm, caused by the fact that the cones have evolved to their full intrinsic heights in agreement with the interaction volume as schematically depicted by the right inset in Figure 2b. So far, it can be concluded that curved surfaces allow for an enhanced electron reemission (BSE and FSE) with a higher contribution of low electron energies which preferably dissociate precursor molecules. This situation is even further increased due to near surface SE generated by the increased number of surface penetration events.

Influence of Precursor Depletion Regime. The comparison of experimental (Figure 2a) and simulated VGR behavior (triangles in Figure 2b) for the sub-100 nm point pitch range reveals that, instead of the simulated progressive increase, a more linear trend is observed for experiments. To explain this behavior, one must consider that the simulations ignore the influence of the precursor coverage which, however, is not constant during the beam dwell time and results in a dynamic growth rate which decreases as the precursor is locally consumed.[29,30,37,54] Depending on the beam dwell time per point, the precursor population *at* but

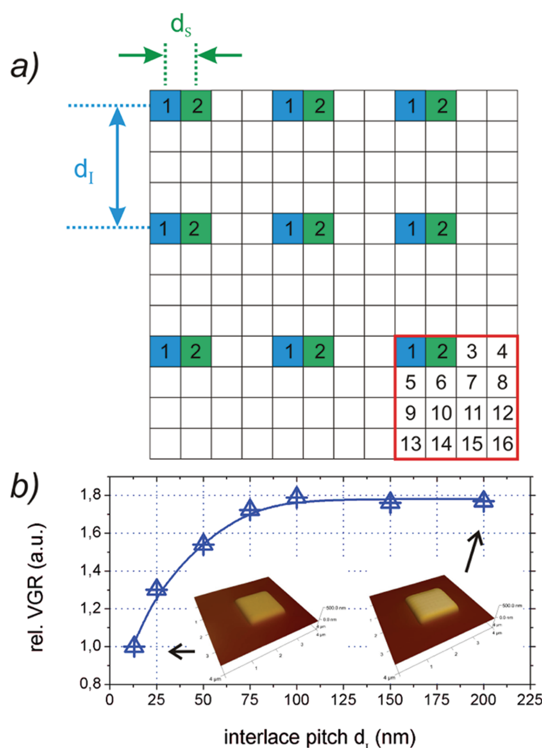

Figure 4. (a) Scheme of interlacing strategy for patterning to combine large point pitches for each single frame while final point pitches are very small; (b) relative volume growth rate behavior for increasing interlace pitches d_I, while final point pitches (d_S) are kept constant at 13 nm. The AFM insets reveal very smooth surfaces for the entire range of d_I (max 1.4 nm rms roughness for 200 nm interlace pitch d_I).

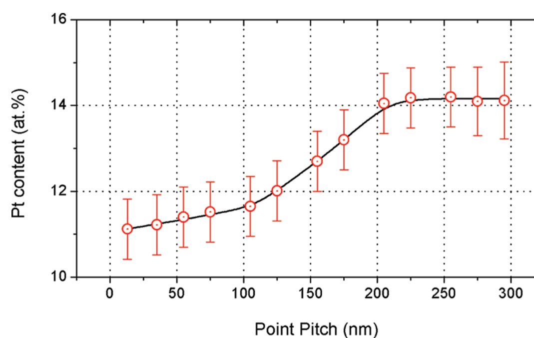

Figure 5. EDS measurements of the Pt content (atom %) dependent on the point pitch values for regular patterning strategies (5 keV, 1600 pA).

also *around* the primary electron beam is depleted due to consumption by different electron species (see Figure S5 and S5). The precursor population is a function of the dynamic depletion and the precursor diffusion and adsorption as replenishment sources, respectively.[29,30,37,54] In particular, the proximity depletion has further consequences if very small point pitches are chosen since consecutive patterning beam pulses will start with partially depleted precursor population. This is equivalent to a growth regime shift toward more mass transport-limited (MTL) conditions[3,5,28] which reduce the VGR. Consequently, larger point pitches provide higher precursor population for consecutive patterning points due to strongly reduced proximity depletion. To separate the growth regime influences from morphology-related proximity effects, discussed in the first part, an interlace patterning strategy was introduced, which is schematically shown in Figure 4a: (1) deposition of one interlace frame with point pitch d_I (blue squares) and low dwell times *t* (needed to provide very flat deposit surfaces after single frame deposition); (2) deposition of the same interlace frame with coordinates shifted about a small distance d_S (green squares). After the sequential execution of several single frames with systematically shifted coordinates, as schematically shown in the red bordered area in Figure 4a, very small final point pitches can be achieved, which deposits flat surfaces. When the interlace point pitch d_I is now systematically increased while the final point pitches are kept identical, proximity depletion described above is continuously reduced while morphological influences are practically eliminated due to very flat deposits. Please note that the total electron dose is kept constant for direct comparison. Figure 4b shows the relative VGR dependency on the interlace point pitch d_I for a constant final point pitch of 13 nm (identical to instrumental default conditions), resulting in deposit roughness of less than 2 nm, as shown by the AFM insets in Figure 4b (1.4 nm rms roughness was found for an interlace point pitch of 200 nm). The important finding, however, is the saturation tendency above 100 nm interlace point pitch which indicates that the proximity depletion for a radius above 100 nm is negligible due to a more constant precursor coverage of the surface. The observed VGR increase above this point pitch in Figure 2a is therefore mainly driven by morphology-induced proximity effects: the increasing electron yield (Figure 2a) in combination with multiple reemission and re-entering processes (Figure 2b).

Chemical Composition. Finally, Figure 5 shows the result of compositional analyses of Pt (atom %) *via* energy-dispersive X-ray spectroscopy (EDS) carefully performed on the dome centers in different geometries. As can be seen, there are three different characteristics: (i) a weak increase, starting with a Pt content of 11 ± 0.7 atom % for 13 nm point pitch, up to about 120 nm where it changes into (ii) a stronger increase up to about 200 nm point pitch followed by (iii) a more constant regime with a Pt content of 14 ± 0.9 atom %. These regimes can be correlated to the varying *electrons per precursor–molecule* ratios. The correlation of the Pt/C ratio in EBID deposits has been well-studied, and the increase in the Pt/C ratios at higher electron currents is associated with more complete dissociation and desorption of carbonaceous byproduct associated with the $MePtCpMe_3$ precursor.[4,56] For point pitch values above 100 nm, the precursor population is

generally constant, as shown by the interlacing experiments in Figure 4b. Conversely, as has been described, the effective electron yield increases with the point pitch and reaches its maximum at about 200 nm (triangles in Figure 2a). Thus the three regimes can be correlated to the effective electron dose per precursor molecule deposited. Starting with region iii, it is clear that above 200 nm point pitch, the precursor population, electron yield, and the effective growth rate all saturate, thus we expect the electron dose/precursor molecule to be constant. In region ii, the precursor population or concentration is generally constant; however, the electron yield is increasing, thus there is an effectively increasing electron dose per precursor molecule in this range. Finally, there is an interesting competition in region i which is attributed to the very gradual change in composition. Namely, both the electron yield (Figure 2a) and the precursor population (Figure 4b) are increasing in this point pitch range due to the depletion range of ~100 nm, thus it appears that the electron yield is increasing at a slightly faster rate than the precursor population is increasing in this range. Thus there appears to be a slightly higher electron dose per precursor molecule in this regime.

Implications for Nanoscale Synthesis. From combined experimental results and simulations, it can be deduced that the VGR variation upon increasing patterning point pitches shown in Figure 2a is mainly driven by two different effects: (i) diffusion based proximity depletion (DPD) for small point pitches which is based on a varying precursor coverage of the surface; and (ii) morphology induced proximity deposition (MPD) for larger point pitches as a result of increasing electron yields and multiple re-emission/re-entering processes on nonflat surfaces, which represent fundamental processes for any type of electron beam induced deposition processes.

The study reveals that re-emission/recollection effects (hence nonlocal deposition) on nonflat surfaces can reach as far as several 100 nm even for low primary electron energy of 5 keV. The practical aspect of these findings and the knowledge of its underlying mechanism is the ability to adapt the deposition process according to the aimed application: (1) DPD effects (low efficiencies) can be minimized by lowering the beam dwell times to a minimum[37,54] (see S5) and the combination with interlacing patterning strategies which enhance VGRs without losing deposit smoothness; (2) MPD influences (unwanted broadening/proximity deposition) can be reduced by lowering the electron energy which effectively reduces the Bethe range and thus the spatial expansion of electron trajectories according to the interaction volume. Alternatively, the electron beam current can be reduced which decreases the number of surface penetrating BSEs and FSEs and as a consequence the fraction of (partly far reaching) recollected/re-emitted electrons.[31,32,37]

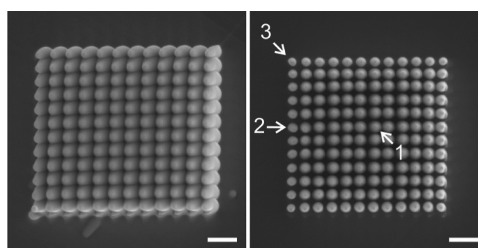

Figure 6. SEM top view images from Pt deposits with 255 nm point pitch for 1600 pA (left) and 400 pA (right).

Figure 6 shows SEM top view images from identically prepared deposits for point pitches of 255 nm and beam currents of 1600 pA (left) and 400 pA (right). It can clearly be seen that the 400 pA structures are not closed due to a reduced number of surface penetrating electrons which can be recollected by adjacent structures. A closer look, however, reveals slightly varying pillar diameter for the 400 pA structure in agreement with previous literature:[31,32] while central pillars are vertically and horizontally almost closed (position 1: Ø ~ 250 nm), positions 2 and 3 reveal systematically reduced diameters of ~200 and ~180 nm. This special finding can be explained by the anisotropy in the number of domes in the vicinity which can contribute to re-emission and recollection: while position 1 has the highest number of neighbors, position 2 has only 50% while position has only 25%. A closer look to the 1600 pA deposit in Figure 6 (left) reveals the same tendencies although more complicated to quantify. These special shapes and variations prove that proximity deposition can be an essential even for the reduced beam current and confirms the validity of the above-discussed model. The laterally varying volume growth rate (Figure 4) based on proximity effects is also capable of explaining why perfectly rectangular cross sections are often complicated to achieve with EBID for mid- and high-range currents.

The observed growth effects, demonstrated here at 5 keV beam energy for PtC_X deposition, have interesting implications for different beam energies and different materials (both of which will be demonstrated in subsequent studies). As described, both proximity effects are a function of the beam interaction region and thus both vary with beam energy and material. However, simply increasing the primary beam energy does not automatically extend the observed trends to larger pitch values due to further effects such as lower dissociation cross sections, different secondary electron generation, and a lower charge carrier density for exiting and re-entering BSE and FSE because the beam interaction region is distributed over larger areas. Thus, as an example, higher currents are expected to be necessary to adequately fill the between-dome regions. Similar arguments can be enumerated for deposited materials with different density, atomic number, and atomic weight. Thus we

present our observations at 5 keV as a basic guide based on a thorough understanding of electron–solid–precursor interactions and suggest that similar trends can be replicated for different beam energies and materials.

CONCLUSIONS

In conclusion, we have investigated the correlation of electron propagation in solids with enhanced volume growth rates for focused electron beam induced deposition processes on nonflat surfaces. Monte Carlo simulations reveal that feature dimensions close to the intrinsic electron interaction volume enhance the electron yield for backscattered and forward scattered electrons which can furthermore be recollected by adjacent surface features (100% collection rate for forward scattered electrons). The data explains in good agreement with experimentally found volume growth rate enhancements which, depending on the purpose, can also result in unwanted proximity deposition or broadening effects. Since the Monte Carlo simulations do not consider the precursor population on the surface, special patterning strategies have been applied to eliminate surface diffusion related depletion effects of precursor molecules, which confirmed the simulation results by means of a surface induced enhancement of the volume growth rates. Finally, the proximity effects were determined to also affect the resultant deposition composition and three regimes were identified and correlated to the effective electron yield per precursor molecule. Importantly, the Pt content increased in the optimum growth strategies presented. The study demonstrates the necessity of a purpose-dependent parameter adaptation during electron beam induced deposition to exploit the full potential of this direct write technique. Furthermore, it is shown how alternative patterning strategies can be used to reduce surface diffusion depletion effects which can be a major issue for electron beam induced deposition processes.

METHODOLOGY

Deposition experiments have been performed with a FEI NOVA 200 dual beam system equipped with a Pt gas injection system (GIS) system (FEI) using $MePtCpMe_3$ as precursor. The substrates were composed of highly oriented pyrolytic graphite (HOPG) which were freshly cleaved *via* adhesive tape immediately before evacuation of the microscope chamber. The Pt precursor was heated at 45 °C at least 1 h prior to deposition, and the GIS nozzle was placed 250 μm above the substrate. To provide a stable thermodynamic precursor/substrate situation, the GIS valve was opened at least 2 min before deposition, resulting in a stable chamber pressure of 2×10^{-5} mbar (microscope chamber background pressure was 6×10^{-6} mbar before the GIS valve was opened). Prior to the actual deposition, a drift compensation field was prepared to establish a charging related equilibrium. Pixel dwell times have been set to 40 μs and kept constant for all experiments. The patterning generator was directly controlled by stream files which have been generated by C++ routines. To analyze the deposit heights, the system was pumped again for at least 1 h after closing the GIS valve and withdrawing the GIS needle. Subsequently, TEOS precursor was used to deposit another layer on top of the Pt deposit to improve contrast of the Pt deposit edge. After another clearance period of 1 h, the focused ion beam capabilities of the dual beam system were used to prepare cross sections of the SiO_x covered Pt deposits *via* low ion beam currents of a maximum of 50 pA. Energy-dispersive X-ray spectroscopy (EDS) was performed in the NOVA 200 system by an Xflash silicon drift detector (4010, Bruker AXS) with short acquisition times of 60 s. To provide high reliability, multiple measurements have been done at the dome centers in different angles to check for morphology-induced artifacts as well as for unwanted carbon contamination. AFM measurements were performed with a Dimension 3100 microscope (Digital Instruments, VEECO) operated with a Nanoscope IVa controller and a Hybrid XYZ closed loop scan-head. The entire system was placed in a glovebox (MBraun Unilab) operated in a dry N_2 atmosphere (H_2O and $O_2 <$ 0.1 ppm).

The Monte Carlo simulations used in this work simulated 1.25 million electrons for each simulation and assumed a 1 nm radius Gaussian shaped electron beam (5 keV) which is introduced to a nondiscretized 3D surface that was calculated based on a prescribed surface; in this case, a series of domes with different height and pitches chosen to represent the resultant EBID morphology realized by varying the scanning parameters. The analytical function describing the surface morphology was derived from TEM and AFM based cross sectional analyses of different point pitch deposits (see S4). Each electron trajectory is calculated using the Bethe continuously slowing down approximation (CSDA) model[57,58] in order to simulate all inelastic scattering events between two elastic events. To estimate scattering angles, a screened Rutherford cross section[59,60] was chosen due to the lack of a more accurate Mott cross section for the PtC_4 and PtC_7 material we were emulating. The stopping power of the material was estimated using Luo and Joy's well-known modified Bethe equation,[61] and the density of the PtC_X deposits was assumed to be ~4.5 and an average *Z* number and molecular weight based on the stoichiometry. This combined approach has been successfully used to solve difficult problems in EBID and EBL applications.[62]

Generation of secondary electrons utilized the fast secondary electron model.[63] This was translated to Monte Carlo code by[64,65] and uses the conservation of momentum and Coulomb interactions between incident electrons and free electrons of the substrate atoms to estimate the number and trajectory of the generated SEs. Their transport to the surface is achieved using a cascade model proposed by[66] which was shown by these authors to provide a very good correlation to experimental yields. The inelastic mean free path (IMFP) of the SEs was estimated using that of PMMA since it has a similar density and high carbon content. The transmission/reflection probability was calculated based on the work of refs 61 and 67. The secondary electron coefficient was tuned for 5 keV beam on a flat PtC_4 and PtC_7 substrate to total secondary electron yield of $PtC_4 = 0.3$ ($SE_I = 0.15$, $SE_{II} = 0.15$) and $PtC_7 = 0.25$ ($SE_I = 0.14$, $SE_{II} = 0.11$) and resulted in a backscattered yield of $PtC_4 = 0.27$ and $PtC_7 = 0.2$. The reduced backscattered and SE yield is attributed to the lower average *Z* number and molecular weight of the PtC_7 material which logically reduces the stopping power. The electrons in the simulation were tracked through space using a single scattering method[59] where they are traced until they exit the sample (and do not re-enter in a space of 4× the prescribed dome pitch) or their energy drops below a set minimum value of 50 eV. Upon their exit, they are tracked as a straight line trajectory through vacuum until they (1) pass the maximum dome height in the *z*-dimension, (2) re-enter a nearby solid

dome, or (3) travel a distance 4× the prescribed pitch in which the trajectory is stopped but they are counted as re-entered if they have a forward scattered trajectory. If they re-enter an adjacent dome, their trajectory is continued using their conserved energy and momentum as demonstrated in the inset of Figure 2b and in more detail in Figure S3c. The simulation stores their exit (and re-entry) energies, radial positions (from the center of the Gaussian source), and angles (relative to the beam direction).

The primary electron (PE) is referred to as a backscattered electron (BSE) if its exit or re-entry trajectory is away from the target sample (*i.e.*, $\phi < 90°$) or a forward scattered (FSE) if it exits or re-enters at a downward trajectory (*i.e.*, $180° > \phi > 90°$). The generated secondary electrons are divided into two classes: SE_I electrons are those which are generated within five scattering steps upon initially entering the sample. SE_{II} electrons are generated at all subsequent scattering steps along the PE trajectory.

For a more detailed explanation of the concepts presented relating to this Monte Carlo model, see ref 28. A comprehensive explanation of these concepts is also given by ref 2.

For the simulations presented in this work, two sets of runs are presented. First, six different types of dome morphologies were run with a pitch of 15, 50, 100, 150, 200, and 250 nm. Each pitch was simulated in such a manner that the PE exit points were stored but tracking through vacuum was disabled, thus stopping the electron solid algorithm upon the first exit. The second set of simulations involved the same pitch series; however, the exited electron trajectory was continued and allowed to re-enter in neighboring domes. Thus a comparison of the electron yields for the primary beam in the incident dome *versus* recollected electrons in neighboring domes could be compared.

Acknowledgment. H.P. gratefully acknowledges support from Prof. Dr. G. Kothleitner and Dr. J. Wagner. P.D.R. and D.A.S. gratefully acknowledge support from Semiconductor Research Corporation (Dan Herr program Manager). P.D.R. also acknowledges that part of his time developing the single scattering Monte Carlo simulation was conducted at the Center for Nanophase Materials Sciences, which is sponsored at Oak Ridge National Laboratory by the Office of Basic Energy Sciences, U.S. Department of Energy.

Supporting Information Available: Additional figures and experimental details. This material is available free of charge *via* the Internet at http://pubs.acs.org.

REFERENCES AND NOTES

1. Randolph, S. J.; Fowlkes, J. D.; Rack, P. D. Focused Nanoscale Electron Beam-Induced Deposition and Etching. *Crit. Rev. Solid State Mater. Sci.* **2006**, *31*, 55–89.
2. Silvis-Cividjian, N.; Hagen, C. W.; Kruit, P. Spatial Resolution Limits in Electron-Beam-Induced Deposition. *J. Appl. Phys.* **2005**, *98*, 8–20.
3. Utke, I.; Hoffmann, P.; Melngailis, J. Gas-Assisted Focused Electron Beam and Ion Beam Processing and Fabrication. *J. Vac. Sci. Technol., B* **2008**, *26*, 1197–1276.
4. van Dorp, W. F.; Hagen, C. W. A Critical Literature Review of Focused Electron Beam Induced Deposition. *J. Appl. Phys.* **2008**, *104*, 081301/1–081301/43.
5. van Dorp, W. F.; van Someren, B.; Hagen, C. W.; Kruit, P.; Crozier, P. A. Approaching the Resolution Limit of Nanometer-Scale Electron Beam-Induced Deposition. *Nano Lett.* **2005**, *5*, 1303–1307.
6. Botman, A.; Mulders, J. J. L.; Hagen, C. W. Creating Pure Nanostructures from Electron-Beam-Induced Deposition using Purification Techniques: A Technology Perspective. *Nanotechnology* **2009**, *20*, 372001/1–372001/18.
7. Toth, M.; Lobo, C. J.; Knowles, W. R.; Phillips, M. R.; Postek, M. T.; Vladar, A. E. Nanostructure Fabrication by Ultra-High-Resolution Environmental Scanning Electron Microscopy. *Nano Lett.* **2007**, *7*, 525–530.
8. Bret, T.; Utke, I.; Gaillard, C.; Hoffmann, P. Periodic Structure Formation by Focused Electron-Beam-Induced Deposition. *J. Vac. Sci. Technol., B* **2004**, *22*, 2504–2510.
9. Udea, K.; Yoshimura, M. Fabrication of Nanofigures by Focused Electron Beam-Induced Deposition. *Thin Solid Films* **2004**, *464*, 331–334.
10. Murukami, K.; Takai, M. Characteristics of Nano Electron Source Fabricated Using Beam Assisted Process. *J. Vac. Sci. Technol., B* **2004**, *22*, 1266–1268.
11. van Dorp, W. F.; Hagen, C. W.; Crozier, P. A.; van Someren, B.; Kruit, P. One Nanometer Structure Fabrication Using Electron Beam Induced Deposition. *Microelectron. Eng.* **2006**, *83*, 1468–1470.
12. Utke, I.; Luisier, A.; Hoffmann, P.; Laub, D.; Buffat, P. A. Focused-Electron-Beam-Induced Deposition of Free-standing Threedimensional Nanostructures of Pure Coalesced Copper Crystals. *Appl. Phys. Lett.* **2002**, *81*, 3245–3247.
13. Liang, T.; Stivers, A.; Livengood, R.; Yan, P. Y.; Zhang, G.; Lo, F. C. Progress in Extreme Ultraviolet Mask Repair Using a Focused Ion Beam. *J. Vac. Sci. Technol., B* **2000**, *18*, 3216–3220.
14. Liang, T.; Stivers, A.; Penn, M.; Bald, D.; Sethi, C.; Boegli, V.; Budach, M.; Edlinger, K.; Spies, P. Demonstration of Damage-Free Mask Repair Using Electron-Beam-Induced Processes. *Proc. SPIE* **2004**, *5446*, 291–300.
15. Liang, T.; Stivers, A. Damage-Free Mask Repair Using Electron Beam Induced Chemical Reactions. *Proc. SPIE* **2002**, *4688*, 375–383.
16. Mayer, J.; Giannuzzi, L. A.; Kamino, T.; Michael, J. TEM Sample Preparation and FIB-Induced Damage. *MRS Bull.* **2007**, *32*, 400–407.
17. El-Awady, J. A.; Woodward, C.; Dimiduk, D. M.; Ghoniem, N. M. Effects of Focused Ion Beam Induced Damages on the Plasticity of Micropillars. *Phys. Rev. B* **2009**, *80*, 104104.
18. Yu, M. F.; Lourie, O.; Dyer, M. J.; Moloni, K.; Kelly, T. F.; Ruoff, R. S. Strength and Breaking Mechanism of Multiwalled Carbon Nanotubes under Tensile Load. *Science* **2000**, *287*, 637–640.
19. Cambria, T. D.; Economou, N. P. Mask and Circuit Repair with Focused-Ion Beam. *Solid State Technol.* **1987**, *30*, 133–136.
20. Edinger, K.; Gotszalk, T.; Rangelow, I. A Novel High Resolution Scanning Thermal Probe. *J. Vac. Sci. Technol., B* **2001**, *19*, 2856–2860.
21. Utke, I.; Hoffmann, P.; Berger, R.; Scandella, L. High Resolution Magnetic Force Microscopy Supertips Produced by Focused Electron Beam Induced Deposition. *Appl. Phys. Lett.* **2002**, *80*, 4792–4794.
22. Shaver, D. C.; Stern, L. A.; Economou, N. P. Mask and Circuit Repair Applications of Focused Ion Beam Deposition. *Microelectron. Eng.* **1986**, *5*, 191.
23. Castagne, M.; Benfedda, M.; Lahimer, S.; Falgayrettes, P.; Fillard, J. P. Near Field Optical Behavior of C Supertips. *Ultramicroscopy* **1999**, *76*, 187–194.
24. Gopal, V.; Radmilovic, V. R.; Daraio, C.; Jin, S.; Yang, P. D.; Stach, E. A. Rapid Prototyping of Site-Specific Nanocontacts by Electron and Ion Beam Assisted Direct-Write Nanolithography. *Nano Lett.* **2004**, *4*, 2059–2063.
25. Danelon, C.; Santschi, C.; Brugger, J.; Vogel, H. Fabrication and Functionalization of Nanochannels by Electron-Beam-Induced Silicon Oxide Deposition. *Langmuir* **2006**, *22*, 10711–10715.
26. Nilsson, J.; Lee, J. R. I.; Ratto, V.; Letant, S. E. Localized Functionalization of Single Nanopores. *Adv. Mater.* **2006**, *18*, 427–431.
27. Reimer, L. *Scanning Electron Microscopy*, 2nd ed.; Springer Series in Optical Sciences, ISBN 3-540-63976-4, Springer: Berlin, 1998; Vol. 45.
28. Smith, D. A.; Fowlkes, J. D.; Rack, P.D. A Nanoscale Three-Dimensional Monte Carlo Simulation of Electron-Beam-Induced Deposition with Gas Dynamics. *Nanotechnology* **2007**, *18*, 265308–265321.
29. Smith, D. A.; Fowlkes, J. D.; Rack, P. D. Simulating the Effects of Surface Diffusion on Electron Beam Induced Deposition *via* a Three-Dimensional Monte Carlo Simulation. *Nanotechnology* **2008**, *19*, 415704–415714.

30. Smith, D. A.; Fowlkes, J. D.; Rack, P. D. Understanding the Kinetics and Nanoscale Morphology of Electron-Beam-Induced Deposition via a Three-Dimensional Monte Carlo Simulation: The Effects of the Precursor Molecule and the Deposited Material. *Small* **2008**, *4*, 1382–1389.
31. Lau, Y. M.; Chee, P. C.; Thong, J. T. L.; Ng, V. Properties and Applications of Cobalt-Based Material Produced by Electron-Beam-Induced Deposition. *J. Vac. Sci. Technol., A* **2002**, *20*, 1295–1302.
32. Bret, T.; Utke, I.; Hoffmann, P.; Abourida, M.; Doppelt, P. Electron Range Effects in Focused Electron Beam Induced Deposition of 3D Nanostructures. *Microelectron. Eng.* **2006**, *83*, 1482–1486.
33. van Dorp, W. F.; van Someren, B.; Hagen, C. W.; Kruit, P. Approaching the Resolution Limit of Nanometer-Scale Electron Beam-Induced Deposition. *Nano Lett.* **2005**, *5*, 1303–1307.
34. Burbridge, D. J.; Gordeev, S. N. Proximity Effects in Free-Standing EBID Structures. *Nanotechnology* **2009**, *20*, 285308–285313.
35. Mitsuishi, K.; Shimojo, M.; Takeguchi, M.; Tanaka, M.; Furuya, K. Effects of Heat Treatment on Electric Properties of Nanorods Formed by Electron Beam-Induced Deposition. *Jpn. J. Appl. Phys.* **2006**, *45*, 5509–5512.
36. Crozier, P. A. Proximity Effects in Nanoscale Patterning with High Resolution Electron Beam Induced Deposition. *J. Vac. Sci. Technol. B* **2008**, *26*, 249–256.
37. Fowlkes, J. D.; Doktycz, M. J.; Rack, P. D. An Optimized Nanoparticle Separator Enabled by Electron Beam Induced Deposition. *Nanotechnology* **2010**, *21*, 165303–165311.
38. Hochleitner, G.; Steinmair, M.; Lugstein, A.; Roediger, P.; Wanzenboeck, H. D.; Bertagnolli, E. Focused Electron Beam Induced Deposition of Gold Catalyst Templates for Si-Nanowires Synthesis. *Nanotechnology* **2011**, *22*, 015302–015306.
39. Guan, Y.; Fowlkes, J. D.; Retterer, S. T.; Simpson, M. L.; Rack, P. D. Nanoscale Lithography *via* Electron Beam Induced Deposition. *Nanotechnology* **2008**, *19*, 505302–505307.
40. Liang, T.; Stivers, A. Damage-Free Mask Repair Using Electron Beam Induced Chemical Reactions. *Proc. SPIE* **2002**, *4688*, 375.
41. Liang, T.; Frendberg, E.; Lieberman, B.; Stivers, A. Advanced Photolithography Mask Repair Using Electron Beams. *J. Vac. Sci. Technol., B* **2005**, *23*, 3101–3105.
42. Nawotec, http://www.smt.zeiss.com/nawotec.
43. Wanzenboeck, H. D.; Fischer, M.; Svagera, R.; Wernisch, J.; Bertagnolli, E. Custom Design of Optical-Grade Thin Films of Silicon Oxide by Direct-Write Electron-Beam-Induced Deposition. *J. Vac. Sci. Technol., B* **2006**, *24*, 2755–2760.
44. Hubner, B.; Koops, H. W. P.; Pagnia, H.; Sotnik, N.; Urban, J.; Weber, M. Tips for Scanning Tunneling Microscopy Produced by Electron-Beam-Induced Deposition. *Ultramicroscopy* **1992**, *42*, 1519–1525.
45. Folks, L.; Best, M. E.; Rice, P. M.; Terris, B. D.; Weller, D.; Chapman, J. N. Perforated Tips for High-Resolution In-Plane Magnetic Force Microscopy. *Appl. Phys. Lett.* **2000**, *76*, 909–911.
46. Akama, Y.; Nishimura, E.; Sakai, A.; Murakami, H. Fabrication of an Electron Beam Deposited AFM Tip and Observation of Submicron Line and Space Pattern. *J. Vac. Sci. Technol., A* **1990**, *8*, 429–433.
47. Wendel, M.; Lorenz, H.; Kotthaus, J. P. Sharpened Electron Beam Induced Tips for High Resolution Atomic Force Microscope Lithography and Imaging. *Appl. Phys. Lett.* **1995**, *67*, 3732–3734.
48. Koops, H. W. P.; Hoinkis, O. E.; Honsberg, M. E. W.; Schmidt, R.; Blum, R.; Böttger, G.; Kuligk, A.; Liguda, C.; Eich, M. Two-Dimensional Photonic Crystals Produced by Additive Nanolithography with Electron Beam-Induced Deposition act as Filters in the Infrared. *Microelectron. Eng.* **2001**, *57−58*, 995–1001.
49. Nellen, P. M.; Callegari, V.; Bronnimann, R. FIB-Milling of Photonic Strutures and Sputtering Simulation. *Microelectron. Eng.* **2006**, *83*, 1805–1808.
50. Roussey, M.; Bernal, M.-P.; Courjal, N.; Baida, F. I. Experimental and Theoretical Characterization of a Lithium Niobate Photonic Crystal. *Appl. Phys. Lett.* **2005**, *87*, 241101–241102.
51. Kometani, R.; Kanda, K.; Haruyama, Y.; Kaito, T.; Matsui, S. Evaluation of Field Electron Emitter Fabricated Using Focused-Ion-Beam Chemical Vapor Deposition. *Jpn. J. Appl. Phys.* **2006**, *45*, 711–713.
52. Boggild, P.; Hansen, T. M.; Tanasa, C.; Grey, F. Fabrication and Actuation of Customized Nanotweezers with a 25 nm Gap. *Nanotechnology* **2001**, *12*, 331–335.
53. Fowlkes, J. D.; Randolph, S. J.; Rack, P.D.n Growth and Simulation of High-Aspect Ratio Nanopillars by Primary and Secondary Electron-Induced Deposition. *J. Vac. Sci. Technol., B* **2005**, *23*, 2825–2832.
54. Plank, H.; Gspan, C.; Dienstleder, M.; Kothleitner, G.; Hofer, F. The Influence of Beam Defocus on Volume Growth Rates for Electron Beam Induced Platinum Deposition. *Nanotechnology* **2008**, *19*, 485302–485311.
55. van Dorp, W. F.; Hagen, C. W. A Critical Literature Review of Focused Electron Beam Induced Deposition. *J. Appl. Phys.* **2008**, *104*, 081301–081342.
56. Van Dorp, W. F.; Wnuk, J. D.; Gorham, J. M.; Fairbrother, D. H.; Madey, T. E.; Hagen, C. W. Electron Induced Dissociation of Trimethyl (Methylcyclopentadienyl) Platinum (IV): Total Cross Section as a Function of Incident Electron Eenergy. *J. Appl. Phys.* **2009**, *106*, 074903/1–074903/9.
57. Bethe, H. A.; Ashkin, J. In *Experimental Nuclear Physics*; Segre, E., Ed.; John Wiley and Sons: New York, 1953.
58. Jablonski, A.; Powell, C. J.; Tanuma, S. Monte Carlo Strategies for Simulations of Electron Backscattering from Surfaces. *Surf. Interface Anal.* **2005**, *37*, 861–874.
59. Joy, D. C. *Monte Carlo Modeling for Electron Microscopy And Microanalysis*; Oxford University Press: New York, 1985; pp 1−216.
60. Newbury, D. E. Electron Beam Specimen Interactions in the Analytical Electron Microscope. In *Principles Of Analytical Electron Microscopy*; Joy, D. C., Romig, A. D., Jr., Goldstein, J. I., Eds.; Plenum: New York, 1986; pp 1−27.
61. Luo, S.; Joy, D. C. Monte Carlo Calculations of Secondary Electron Emission. *Scanning Microsc. Suppl.* **1990**, *4*, 127–146.
62. Ho, Y.; Tan, Z.; Wang, X.; Chen, J. A Theory and Monte Carlo Calculation on Low-Energy Electron Scattering. *Scanning Microsc.* **1991**, *5*, 945–951.
63. Joy, D. C. Beam Interactions, Contrast and Resolution in the SEM. *J. Microsc.* **1984**, *136*, 241–258.
64. Koshikawa, T.; Shimizu, R. A Monte Carlo Calculation of Low-Electron Secondary Electron Emission from Metals. *J. Phys. D* **1974**, *7*, 1303–1315.
65. Kotera, M. A Monte Carlo Simulation of Primary and Secondary Electron Trajectories in a Specimen. *J. Appl. Phys.* **1989**, *65*, 3991–3998.
66. Ding, Z. J.; Shimizu, R. Monte Carlo Simulation Study of Secondary Electron Emission and Surface Excitation. Inst. Phys. Conf. Ser. No. 165: Symposium 8, 2nd Conf. Int. Union Microbeam Analysis Societies, Kailua-Kona, Hawaii, 9−13 July; IOP Publishing Ltd.: London, 2000; pp 279−295.
67. Luo, S.; Zhang, Y.; Wu, Z. A Monte Carlo Calculation of Secondary Electrons Emitted from Au, Ag, and Cu. *J. Microsc.* **1987**, *148*, 289–295.